How is the ocean filled?

Geoffrey Gebbie[1] and Peter Huybers[2]

Received 13 January 2011; revised 4 February 2011; accepted 15 February 2011; published 23 March 2011.

[1] The ocean surface rapidly exchanges heat, freshwater, and gases with the atmosphere, but once water sinks into the ocean interior, the inherited properties of seawater are closely conserved. Previous water-mass decompositions have described the oceanic interior as being filled by just a few different property combinations, or water masses. Here we apply a new inversion technique to climatological tracer distributions to find the pathways by which the ocean is filled from over 10,000 surface regions, based on the discretization of the ocean surface at 2° by 2° resolution. The volume of water originating from each surface location is quantified in a global framework, and can be summarized by the estimate that 15% of the surface area fills 85% of the ocean interior volume. Ranked from largest to smallest, the volume contributions scaled by surface area follow a power-law distribution with an exponent of -1.09 ± 0.03 that appears indicative of the advective-diffusive filling characteristics of the ocean circulation, as demonstrated using a simple model. This work quantifies the connection between the surface and interior ocean, allowing insight into ocean composition, atmosphere-ocean interaction, and the transient response of the ocean to a changing climate.
Citation: Gebbie, G., and P. Huybers (2011), How is the ocean filled?, *Geophys. Res. Lett.*, *38*, L06604, doi:10.1029/2011GL046769.

1. Introduction

[2] Traditionally, a handful of water masses having distinct hydrographic properties are called upon to describe the composition of the ocean [e.g., *Wüst*, 1935; *Warren*, 1981], where each water mass is defined by a characteristic set of temperature, salinity, and other hydrographic properties. The oceanic volume occupied by each water mass is typically estimated by inverting hydrographic measurements [e.g., *Tomczak*, 1981; *Mackas et al.*, 1987; *Tomczak and Large*, 1989], but the results have proven sensitive to the number and definition of the water masses. For example, *Broecker et al.* [1998] used one hydrographic property to distinguish between North Atlantic Deep Water and Antarctic Bottom Water, finding that they contributed equally to filling the deep Pacific. More recently, *Johnson* [2008] decomposed the subthermocline world ocean into seven water masses and found that Antarctic Bottom Water fills two to three times more of the deep Pacific than North Atlantic Deep Water. Another answer might be obtained if more water masses were included, but traditional inverse approaches are limited to distinguishing only as many water masses as there are distinct water properties, and there is little prospect of obtaining enough well-measured global tracers to resolve this issue using previous methods.

2. Method

[3] To circumvent this methodological roadblock, we extend and apply a recently developed inverse technique [*Gebbie and Huybers*, 2010], referred to as Total Matrix Intercomparison (TMI). Like other water mass decompositions [e.g., *Tomczak*, 1999], TMI is based upon inverting tracer conservation equations, but it is unique to this class of methods in that it also accounts for the geography interconnecting the tracer observations in a more complete way. More specifically, TMI diagnoses the pathways that connect each interior box to every surface region of a discretized ocean by following trails of similar water properties, where directionality is determined using the telltale signs of nutrient remineralization. Instead of solving for water masses that are defined by water properties, we seek a solution in terms of water origins, where we distinguish waters last in contact with a specific surface region of the ocean. TMI yields an estimate of the interior ocean volume filled from every surface gridbox resolved in a given dataset, thus permitting a more detailed quantification than previously available from observations.

[4] Each surface box is a source of water with a particular set of property values, and as such, can be considered a "water type" as defined by *Tomczak and Large* [1989]. Many surface boxes have similar properties, and thus, interior ocean waters cannot be distinguished by these relatively minor differences. The crucial additional step in this study is to identify waters by their surface origin, and to trace the constituents of each interior water back to the surface location from which they originated. The degree to which waters from adjacent locations can be distinguished is addressed later.

[5] The information content in TMI is encapsulated in the pathways matrix, **A**, derived fully by *Gebbie and Huybers* [2010] and reviewed here. To obtain the matrix, we first solve for the mass contribution made to each box by each of its immediate neighbors using the same form as a traditional water-mass decomposition. In steady state, the tracer concentration in each box must satisfy, $c_o = m_1 c_1 + m_2 c_2 + \ldots + q$, where the m's give the fractional mass contribution and q represents internal sources for nonconservative tracers, related by stoichiometric ratios of 1:15.5:-170 for phosphate, nitrate, and oxygen concentrations [*Anderson and Sarmiento*, 1994]. Each box has up to six neighbors and a biological source term, giving seven unknowns constrained by the six observed tracers and mass conservation. For ease of notation, the m_i and q unknown terms are combined in the vector, **x**. Using a weighted, tapered, non-negative least squares

[1]Department of Physical Oceanography, Woods Hole Oceanographic Institution, Woods Hole, Massachusetts, USA.
[2]Department of Earth and Planetary Sciences, Harvard University, Cambridge, Massachusetts, USA.

0094-8276/11/2011GL046769

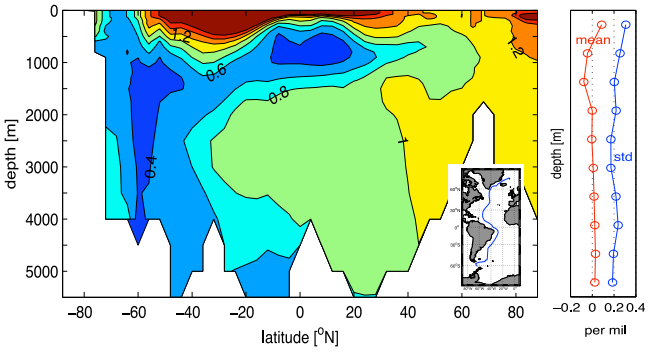

Figure 1. A check of the skill of the TMI method. (left) Section of estimated δ^{13}C from the TMI method along the western Atlantic GEOSECS track (inset map). (right) The mean difference (red) and standard deviation of the misfit (blue) between the TMI estimate and observations, calculated in 500 meter bins, and plotted as a function of depth.

method [*Lawson and Hanson*, 1974], we solve the matrix equation at each location: $\mathbf{Ex} + \mathbf{n} = \mathbf{y}$, where $\mathbf{E}$ is a square matrix, $\mathbf{n}$ is noise, and $\mathbf{y}$ is the observations. The weighting accounts for data accuracy, and the non-negativity constraint enforces mass contributions and nonconservative sources to be zero or greater. The local information is aggregated into a single matrix equation, $\mathbf{Ac} = \mathbf{d}$, where $\mathbf{A}$ contains the m's from the local inversion, $\mathbf{c}$ is any tracer distribution, and $\mathbf{d}$ provides the surface boundary conditions and interior source terms. The global matrix $\mathbf{A}$ is square, full rank, and encapsulates the influence of any ocean grid box on any other.

[6] The principles underlying TMI are straightforward, but several complexities must be dealt with. To account for the effects of the seasonal cycle, we apply TMI to observations that represent late wintertime conditions by requiring that the ocean be well-mixed above the seasonally-maximum mixed-layer depth, as this depth is most indicative of the properties transmitted into the ocean interior [*Stommel*, 1979]. Longer-term variations due to natural ocean-atmosphere variability and anthropogenic changes [*Johnson and Orsi*, 1997; *Curry and Mauritzen*, 2005] are treated by allowing uncertainty in the surface tracer concentrations that are explicitly solved for. In the rare (<0.01%) case that climatological tracer distributions do not provide enough independent information, we seek the circulation with the minimum amount of diapycnal mixing that still fits the observations. Furthermore, small-scale pathways along the ocean bottom are crucial for obtaining a realistic circulation, and thus, sub-gridscale bottom flows off of continental shelves and through mid-ocean fracture zones are allowed (see *Gebbie and Huybers* [2010] for more detail).

[7] We train TMI with the WOCE climatology of temperature, salinity, phosphate, nitrate, and oxygen [*Gouretski and Koltermann*, 2004] and the GISS oxygen-18/oxygen-16 isotope ratio [*LeGrande and Schmidt*, 2006] resolved at 2° × 2° in the horizontal and 33 levels in the vertical. The result is a steady-state circulation estimate that fits the 1,746,936 tracer observations within their reported uncertainties (see Figure S1 in auxiliary material).[1] As a more stringent test, we also analyze the consistency of this circulation estimate with a tracer distribution withheld from the inversion, the GEOSECS δ^{13}C observations [*Craig and Turekian*, 1980], where the influence of biological fractionation of carbon is accounted for by a 1.1‰ decrease in δ^{13}C for each 1 μmol/kg increase in phosphate [*Broecker and Maier-Reimer*, 1992]. The foregoing circulation estimate fits the withheld δ^{13}C observations to within a standard error of approximately 0.2‰ at each depth level, consistent with the expected measurement error and interlaboratory offsets inherent to the data (Figure 1), suggesting robustness. As a side benefit, TMI also yields a global estimate of the distribution of δ^{13}C that should be superior to standard estimates that assume isotropic spatial covariance. Additional tests of TMI using synthetic model data also indicate substantial skill (see the auxiliary material).

3. The Surface Origin of the Interior Ocean

[8] To estimate where all interior ocean waters were last in communication with the surface, we track backward along each pathway from the interior to the surface by means of an extension to the TMI methodology. The total volume, $\mathbf{V}_{tot}$, originating from a surface box could be calculated by dyeing the surface box and summing the product of the dye concentration and the volume of each gridbox. This calculation, however, is computationally intensive because each surface location must be dyed in succession, and instead we use the fact that $\mathbf{V}_{tot}$ is equal to the inverse transpose of the $\mathbf{A}$ matrix multiplied by a vector, $\mathbf{v}$, containing gridbox volumes: $\mathbf{V}_{tot} = \mathbf{A}^{-T}\,\mathbf{v}$. This expression is derived as a sensitivity or "adjoint" problem that gives all the relevant information in one calculation (see auxiliary material for the derivation).

[9] The number of surface origin sites that can be distinguished is only limited by the underlying spatial resolution of the dataset and independence of the observations at that resolution. One external parameter, the tapering coefficient α, is added to TMI to remedy any lack of independence in observations at 2° resolution. We find that the gridscale variability and degree of smoothness of Figure 2 is sensitive to this choice. Here, the strength of the tapering is deter-

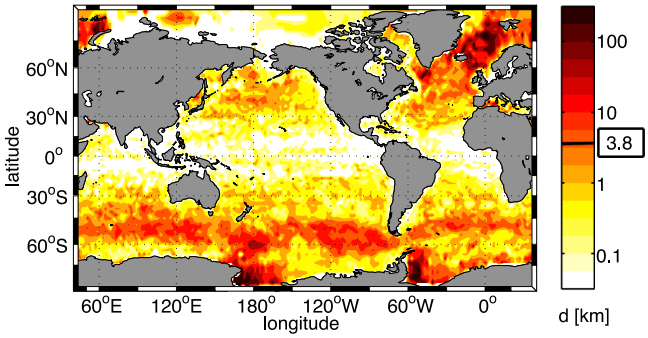

Figure 2. The surface sources of global ocean waters. Oceanic volume that has originated in each 2° by 2° surface location (11,113 origination sites), scaled by the surface area of each box to make an equivalent thickness, d. The color-scale follows a base-ten logarithm of the field. For reference, the colorbar includes the average depth of the ocean (3.8 km), equal to the area-weighted mean of d.

[1] Auxiliary materials are available in the HTML. doi:10.1029/2011GL046769.

Table 1. The Effective Endmembers That Fill the Ocean Averaged Into 7 Regions, and the Fraction of Ocean Property Variability Below 1000 Meters Depth That They Explain[a]

	ANT	NATL	SUBANT	NPAC	ARC	MED	TROP	11,113	7
θ [°C]	−1.31	2.64	5.09	5.43	−0.89	16.38	17.35	99.8	74.6
Sal. []	34.62	34.88	34.25	33.25	34.45	38.03	35.43	96.6	91.1
δ^{18}O [VSMOW]	−0.20	0.27	−0.21	−0.55	0.03	1.37	0.46	81.7	78.3
PO_4[$\mu mol/kg$]	2.11	0.84	1.62	1.41	1.09	0.13	0.45	99.1	98.8
NO_3[$\mu mol/kg$]	29.7	12.9	23.7	18.1	7.6	1.6	4.7	99.2	99.1
O_2[$\mu mol/kg$]	283	308	279	291	332	239	233	99.0	98.2

[a]The seven regions are the Antarctic, North Atlantic, Subantarctic, North Pacific, Arctic, Mediterranean, and Tropics (see auxiliary material for a map). The last two columns on the right-hand side indicate the percent variance explained for each property using the full TMI solution with 11,113 distinct origination sites, and that explained using seven effective endmembers. Note that PO_4, NO_3, and O_2 fractions are computed in both cases using the nonconservative effects estimated from TMI, whose importance accounts for the uniformly high fraction of variance explained.

mined by the signal-to-noise ratio in the tracer observations [*Hansen*, 1992], implemented so as to minimize diapycnal mixing while guarding against fitting noise in the observations (see the auxiliary material for details).

[10] Our estimate of the origin of interior waters averages across all production and destruction of waters over the equilibration time of the ocean—from decades to millennia depending upon location—and is, therefore, complementary to other estimates of water-mass formation that focus on seasonal and interannual timescales [e.g., *Khatiwala et al.*, 2002]. While water-mass formation rates have been previously estimated on a regional basis, such as the Southern Ocean [e.g., *Orsi et al.*, 1999, 2002], we produce a map on a global scale where the relative contributions are assessed in a consistent framework. Furthermore, we emphasize that TMI produces an estimate of effective formation, the net effect of formation and destruction, which is the relevant quantity for assessing global inventories on climatic timescales. As expected, important sites for filling the ocean exist in the North Atlantic, Weddell Sea, and Ross Sea (Figure 2). A prolific band of source regions also exists around the Antarctic Circumpolar Current, near 55°S, in accord with the documented importance of Subantarctic Mode Water and Antarctic Intermediate Water in ventilating the Southern Hemisphere [e.g., *McCartney*, 1977; *Piola and Georgi*, 1982]. Even though these Subantarctic waters have a relatively low density, they are irreversibly mixed with waters originating from the Antarctic region and upwelled waters originating from the North Atlantic. Once mixed, their journeys throughout the world ocean are intertwined and, thus, relatively light waters can have a significant presence at great depths [*Worthington*, 1981]. The estimated high contribution from regions of the Arctic, such as the Barents Sea, is sensitive to the assumed depth of the mixed layer. Note that contact with the atmosphere does not necessarily imply complete equilibration with overlying atmospheric conditions so that water properties may be indicative of exchanges at multiple locations, though for purposes of specificity we focus on the most recent exchange.

[11] While the interior ocean is made up of waters from many different surface sites, just a few property combinations may explain much of the ocean interior, as recognized by many previous water-mass studies [e.g., *McCartney and Talley*, 1982; *Johnson*, 2008]. A major issue is the choice of the properties themselves and interpreting what they mean. Here, TMI permits calculation of the most representative properties for a particular surface region, where the "effective endmembers" are given by the surface concentrations weighted by the volume filled by each location. Splitting the surface ocean into 7 regions (given by Figure S2 in the auxiliary material), we find that the North Atlantic surface region is characterized by $\theta = 2.64$°C and S = 34.88, while the Antarctic region is $\theta = -1.31$°C and S = 34.62, values that are similar to those traditionally used to describe NADW and AABW (see Table 1 for a complete list of endmembers). To determine how well the 7-region solution can explain interior tracer distributions, we propagate the endmember values into the interior by use of the regional water-mass fraction maps of *Gebbie and Huybers* [2010]. The TMI method with 11,113 surface sites explains 99.8% of the global temperature variability below 1000 meters depth, while the 7 endmember solution explains 74.6%, an adequate amount for many applications. For salinity, 96.6% of the variance is explained by the 11,113 surface sites, whereas 91.1% is explained by the 7 endmembers. Although a large number of surface sites fill the ocean, the number of property combinations that are needed to explain the majority of ocean tracer variability is much smaller.

4. Power-Law Description of Ocean Filling

[12] The percentage of water filled from a given surface site clearly depends on the spatial resolution of the dataset, so our results are discussed in terms that take surface area into account. We estimate that 85% of the ocean volume originates from 15% of the global surface area, a ratio reminiscent of the 80–20 rule-of-thumb (or Pareto principle) in statistics. When TMI is applied to the dataset that is block-averaged at 4° horizontal resolution, the estimate is very similar at 86%–14%. To display the spatial pattern of how the ocean is filled, we introduce an equivalent thickness, d, defined as the filled volume of the interior ocean divided by the area of a given surface patch. By definition, the average d across all surface points equals the average depth of the ocean. When ranked from largest to smallest, the equivalent thickness filled from successive surface patches follows a simple power-law distribution,

$$d_n = d_o n^{-p}, \tag{1}$$

where d_o equals 9.2×10^7 m, the d_n are arranged from largest to smallest, and n ranges from 1 to 11,113. Equation (1) is known as a Zipf distribution [*Newman*, 2005], and a maximum likelihood estimate [*Clauset et al.*, 2007] gives $p = 1.09 \pm 0.03$ (Figure 3, top). The estimate is statistically valid for the first 1,250 points, i.e., $n = 1250$ (black line in Figure 3, top). The distribution of d_n falls off more rapidly than n^{-p} for

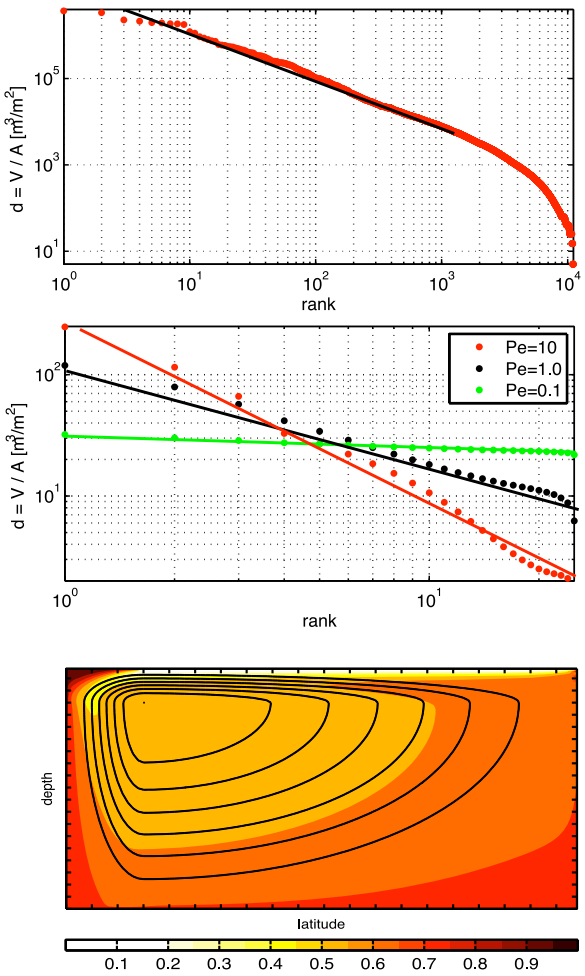

Figure 3. The distribution of volume contributions from 11,113 surface sites. (top) The distribution of equivalent thickness ordered from largest to smallest (red dots) with the best-fit power law (black line). If the x-axis is replaced by the cumulative fraction of ocean area, the plot is not visibly changed. (middle) A rank-size diagram of the same form as the top panel, but for an idealized advection-diffusion model of an overturning circulation. (bottom) The overturning streamfunction (black lines) of the idealized model with the fraction of water originating from the left-most five surface gridpoints (background color).

$n > 1250$. One could also fit the 100 most important points with a power law with a shallower slope closer to $p = 1$, although it does not have the statistical significance of our first fit. Repeating the analysis at 4° × 4° resolution results in a similar distribution once differences in surface area are accounted for (see Figure S3 in auxiliary material), reflecting the scale invariance associated with power-law processes.

[13] Some further insight into the controls upon the equivalent thickness distribution can be obtained from a simple tracer model containing an advective two-dimensional overturning cell and horizontal diffusion. The model produces a power-law scaling in equivalent thickness similar to that of the observations (Figures 3, middle and 3, bottom). The power-law slope is a function of the model's Peclet number; for example, decreasing the rate of advection relative to diffusion increases the breadth of surface sources entrained in downwelling fluid and gives a flatter distribution of d_n. Entrainment of diffusively mixed ambient fluid is expected from dynamical studies of ocean convection [*Jones and Marshall*, 1993] and gravity currents [*Hughes and Griffiths*, 2006]. Even if the advective velocity field indicates a small sinking region, it is possible to have a wide range of contributing surface regions.

5. Discussion and Conclusions

[14] The interpretation of the ocean as being filled by just a handful of sinking regions [*Stommel and Arons*, 1960; *Stommel*, 1962] was an idealized construct, and there is observational evidence for at least a few tens of waters that fill the ocean [e.g., *Gordon*, 1974; *Talley and Raymer*, 1982; *McCartney and Talley*, 1982; *Hanawa and Talley*, 2001; *Yashayaev and Clarke*, 2008]. Nonetheless, numerical tools for dealing with more than ten water masses have been lacking, essentially requiring observational studies to assume just a few surface regions contribute to filling the interior [e.g., *Stuiver et al.*, 1983; *Matsumoto*, 2007]. Here we quantify how the ocean is filled at 2° resolution through the inversion of most of the available ocean tracer data. Prior to this work, only numerical models [*Haine and Hall*, 2002; *Primeau*, 2005] or data assimilation products [e.g., *Schlitzer*, 2007] could provide a picture of how the ocean is filled at this resolution.

[15] Furthermore, we find that the volume filled by each surface box generally follows a power-law distribution, when ranked from highest to lowest. The shallow slope of the power law, which we suggest is set by the ratio of advective and diffusive processes, indicates that the ocean is filled from a broad number of surface locations. Specifically, 15% of the ocean surface fills 85% of the interior. Nonetheless, it is possible to describe much of the variability in interior property distributions using small numbers of property combinations due to regional homogeneities. The power-law scaling of ocean filling is rather simple given the various controls upon water formation, including brine rejection in polar regions, gravitational instability of deep water formation in subpolar regions, and wind-induced subduction in the subtropics. It will be useful to explore the degree to which this power law holds in the presence of changes in ocean energetics, stratification, and bathymetry. The more detailed quantification of the relationship between surface properties and the interior composition of the ocean should also facilitate study of how variations in interior water-mass properties [e.g., *Johnson et al.*, 2007] relate to surface climate.

[16] **Acknowledgments.** GG and PH were funded by NSF award 0645936. GG was also supported by the J. Lamar Worzel Assistant Scientist Fund and the Penzance Endowed Fund in Support of Assistant Scientists. PH was also supported by NSF award OCE-0960787. We thank Carl Wunsch, Andrew Rhines, Luke Skinner, and two anonymous reviewers for constructive comments. We also thank Bruce Warren for his feedback and dedicate this work to him.

[17] The Editor thanks two anonymous reviewers for their assistance in evaluating this paper.

References

Anderson, L. A., and J. L. Sarmiento (1994), Redfield ratios of remineralization determined by nutrient data analysis, *Global Biogeochem. Cycles*, *8*(1), 65–80.

Broecker, W. S., and E. Maier-Reimer (1992), The influence of air and sea exchange on the carbon isotope distribution in the sea, *Global Biogeochem. Cycles*, *6*(3), 315–320.

Broecker, W. S., et al. (1998), How much deep water is formed in the Southern Ocean?, *J. Geophys. Res.*, *103*(C8), 15,833–15,843.

Clauset, A., C. Shalizi, and M. Newman (2007), Power-law distributions in empirical data, *SIAM Rev.*, *51*(4), 661–703.

Craig, H., and K. K. Turekian (1980), The GEOSECS program—1976–1979, *Earth Planet. Sci. Lett.*, *49*(2), 263–265.

Curry, R., and C. Mauritzen (2005), Dilution of the northern North Atlantic Ocean in recent decades, *Science*, *308*(5729), 1772–1774.

Gebbie, G., and P. Huybers (2010), Total matrix intercomparison: A method for resolving the geometry of water-mass pathways, *J. Phys. Oceanogr.*, *40*(8), 1710–1728.

Gordon, A. (1974), Varieties and variability of Antarctic Bottom Water, *Colloq. Int. C. N. R. S.*, *215*, 33–47.

Gouretski, V., and K. Koltermann (2004), WOCE global hydrographic climatology, *Tech. Rep. 35*, Ber. des Bundesamtes für Seeschifffahrt und Hydrogr., Hamburg, Germany.

Haine, T. W. N., and T. M. Hall (2002), A generalized transport theory: Water-mass composition and age, *J. Phys. Oceanogr.*, *32*(6), 1932–1946.

Hanawa, K., and L. Talley (2001), Mode waters, in *Ocean Circulation and Climate: Observing and Modelling the Global Ocean*, *Int. Geophys. Ser.*, vol. 77, pp. 373–386, Academic, San Diego, Calif.

Hansen, P. C. (1992), Analysis of discrete ill-posed problems by means of the L-curve, *SIAM Rev.*, *34*(4), 561–580.

Hughes, G., and R. Griffiths (2006), A simple convective model of the global overturning circulation, including effects of entrainment into sinking regions, *Ocean Modell.*, *12*(1–2), 46–79.

Johnson, G. C. (2008), Quantifying Antarctic Bottom Water and North Atlantic Deep Water volumes, *J. Geophys. Res.*, *113*, C05027, doi:10.1029/2007JC004477.

Johnson, G. C., and A. H. Orsi (1997), Southwest Pacific Ocean water-mass changes between 1968/69 and 1990/91, *J. Clim.*, *10*(2), 306–316.

Jones, H., and J. Marshall (1993), Convection with rotation in a neutral ocean: A study of open-ocean deep convection, *J. Phys. Oceanogr.*, *23*, 1009–1039.

Khatiwala, S., P. Schlosser, and M. Visbeck (2002), Rates and mechanisms of water mass transformation in the Labrador Sea as inferred from tracer observations, *J. Phys. Oceanogr.*, *32*(2), 666–686.

Lawson, C. L., and R. J. Hanson (1974), *Solving Least-Squares Problems*, Prentice Hall, Englewood Cliffs, N. J.

LeGrande, A. N., and G. A. Schmidt (2006), Global gridded data set of the oxygen isotopic composition in seawater, *Geophys. Res. Lett.*, *33*, L12604, doi:10.1029/2006GL026011.

Mackas, D. L., K. L. Denman, and A. F. Bennett (1987), Least squares multiple tracer analysis of water mass composition, *J. Geophys. Res.*, *92*(C3), 2907–2918.

Matsumoto, K. (2007), Radiocarbon-based circulation age of the world oceans, *J. Geophys. Res.*, *112*, C09004, doi:10.1029/2007JC004095.

McCartney, M. (1977), Subantarctic mode water, in *A Voyage of Discovery: George Deacon 70th Anniversary Volume, Supplement to Deep-Sea Research*, edited by M. V. Angel, pp. 103–119, Pergamon, Oxford, U. K.

McCartney, M., and L. Talley (1982), The subpolar mode water of the North Atlantic Ocean, *J. Phys. Oceanogr.*, *12*(11), 1169–1188.

Newman, M. (2005), Power laws, Pareto distributions and Zipf's law, *Contemp. Phys.*, *46*(5), 323–351.

Orsi, A. H., G. C. Johnson, and J. L. Bullister (1999), Circulation, mixing, and production of Antarctic Bottom Water, *Prog. Oceanogr.*, *43*(1), 55–109.

Orsi, A. H., W. M. Smethie Jr., and J. L. Bullister (2002), On the total input of Antarctic waters to the deep ocean: A preliminary estimate from chlorofluorocarbon measurements, *J. Geophys. Res.*, *107*(C8), 3122, doi:10.1029/2001JC000976.

Piola, A., and D. Georgi (1982), Circumpolar properties of Antarctic Intermediate Water and Subantarctic Mode Water, *Deep Sea Res., Part A*, *29*(6), 687–711.

Primeau, F. (2005), Characterizing transport between the surface mixed layer and the ocean interior with a forward and adjoint global ocean transport model, *J. Phys. Oceanogr.*, *35*(4), 545–564.

Schlitzer, R. (2007), Assimilation of radiocarbon and chlorofluorocarbon data to constrain deep and bottom water transports in the world ocean, *J. Phys. Oceanogr.*, *37*(2), 259–276.

Stommel, H. (1962), On the smallness of sinking regions in the ocean, *Proc. Natl. Acad. Sci. U. S. A.*, *48*(5), 766–772.

Stommel, H. (1979), Determination of water mass properties of water pumped down from the Ekman layer to the geostrophic flow below, *Proc. Natl. Acad. Sci. U. S. A.*, *76*, 3051–3055.

Stommel, H., and A. B. Arons (1960), On the abyssal circulation of the world ocean. II. An idealized model of the circulation pattern and amplitude in oceanic basins, *Deep Sea Res.*, *6*, 217–233.

Stuiver, M., P. D. Quay, and H. G. Ostlund (1983), Abyssal water C-14 distribution and the age of the world oceans, *Science*, *219*(4586), 849–851.

Talley, L. D., and M. E. Raymer (1982), Eighteen degree water variability, *J. Mar. Res.*, *49*, 755–775.

Tomczak, M. (1981), A multi-parameter extension of temperature/salinity diagram techniques for the analysis of non-isopycnal mixing, *Prog. Oceanogr.*, *10*(3), 147–171.

Tomczak, M. (1999), Some historical, theoretical and applied aspects of quantitative water mass analysis, *J. Mar. Res.*, *57*(2), 275–303.

Tomczak, M., and D. G. B. Large (1989), Optimum multiparameter analysis of mixing in the thermocline of the eastern Indian Ocean, *J. Geophys. Res.*, *94*(C11), 16,141–16,149.

Warren, B. A. (1981), Deep circulation of the world ocean, in *Evolution of Physical Oceanography, Scientific Surveys in Honor of Henry Stommel*, edited by B. A. Warren and C. Wunsch, pp. 6–41, MIT Press, Cambridge, Mass.

Worthington, L. (1981), The Water Masses of the World Ocean: Some Results of a Fine-Scale Census, in *Evolution of Physical Oceanography, Scientific Surveys in Honor of Henry Stommel*, edited by B. A. Warren and C. Wunsch, pp. 42–60, MIT Press, Cambridge, Mass.

Wüst, G. (1935), Schichtung und zirkulation des Atlantischen Ozeans. Die stratosphare, in *The Stratosphere of the Atlantic Ocean*, edited by W. J. Emery, pp. 1–180, U.S. Dep. of Commer., Springfield, Va.

Yashayaev, I., and A. Clarke (2008), Evolution of North Atlantic water masses inferred from Labrador Sea salinity series, *Oceanography*, *21*(1), 30–45.

G. Gebbie, Woods Hole Oceanographic Institution, MS 29, Woods Hole, MA 02543, USA. (ggebbie@whoi.edu)

P. Huybers, Department of Earth and Planetary Sciences, Harvard University, Cambridge, MA 02138, USA.

Auxiliary Material Submission for manuscript

"How is the ocean filled?"

Geoffrey Gebbie

Physical Oceanography Department, Woods Hole Oceanographic Institution

Peter Huybers

Department of Earth and Planetary Sciences, Harvard University

Contents

The total matrix intercomparison (TMI) method [*Gebbie and Huybers*, 2010] seeks the steady-state circulation that best fits modern-day tracer climatologies. The datasets include the WOCE tracer climatologies of temperature, salinity, phosphate, nitrate, and oxygen [*Gouretski and Koltermann*, 2004], as well as the GISS oxygen-18/oxygen-16 isotope ratio climatology [*Legrande and Schmidt*, 2006]. The search for a steady-state circulation is formalized as the least-squares problem of minimizing a sum of squared misfits between estimated and observed tracer distributions,

$$\mathrm{J} = (\mathbf{E}\mathbf{x} - \mathbf{y})^T (\mathbf{E}\mathbf{x} - \mathbf{y}) + \mu^T \mathcal{F}[\mathbf{x}], \tag{1}$$

where $\mathbf{x}$ is the state vector, $\mathbf{y}$ contains a suite of tracer observations, $\mathbf{E}$ is a matrix that maps the state vector onto the observations, T is the matrix transpose, μ is a Lagrange multiplier vector, and $\mathcal{F}[\mathbf{x}] = 0$ is the steady-state circulation constraint. The Lagrange multiplier term enforces the steady-state circulation requirement. Similar formulations have been used in the past [*Schlitzer*, 2007].

1. The steady-state circulation

First, we show a novel way to formulate the steady-state constraint and to solve for the steady-state circulation. In steady-state, a conservative tracer concentration in an interior box must be a linear combination of the tracer concentrations in neighboring boxes:

$$c_o = \sum_{i=1}^{6} m_i c_i \tag{2}$$

where the summation goes to 6 because there are 6 neighbors in three dimensions, and m_i is the volume (or nearly equivalently, mass) fraction from each neighboring box. In the case that a tracer is nonconservative, a source term must be added to the right hand side. This tracer equation can be rearranged such that all the terms are on the left hand side and the equation is equal to zero. Appending one equation for each interior point, we arrive at the operator $\mathcal{F}[\mathbf{x}]$, where the state vector $\mathbf{x}$ now includes all of the tracer distributions and the m_i mass fraction values.

The operator $\mathcal{F}$ is highly nonlinear as the state vector unknowns multiply each other. If we linearize about the observed tracer values, which is possible because we have complete gridded datasets for the tracers, then it is possible to solve for the mass fraction values between all interior boxes. To solve this subproblem, we have a non-negative least squares problem at every interior location, and it is set up so that there are seven constraints (tracer conservation equations plus mass conservation) and, at most, seven unknowns (6 mass fractions plus a nonconservative source term). The local sub-problem appears to be mathematically well-posed. In practice, some tracer information may not be independent, and thus we use a tapered and weighted least squares method to seek the the circulation with the minimum amount of diapycnal mixing that still fits the observations. The additional constraint is specified as a tapering of the least-squares solution, where the strength of the tapering is determined by the signal-to-noise ratio in the tracer observations [*Hansen*, 1992]. This approach regularizes the TMI matrix to produce a unique solution for the global pathways and guards against overfitting noise in the observations.

Putting all of the m_i values together, we form a linearized steady-state matrix, $\mathbf{F}$.

Multiplying the matrix by a vectorized tracer distribution, **Fc**, gives the imbalance from steady-state. If we append surface boundary conditions to **F**, we obtain the TMI pathways matrix **A**, discussed in Gebbie & Huybers (2010). Obtaining **A** is the first step of a 2-step inversion process.

There are a number of intricacies in finding **A** successfully. First, provisions must be made along the seafloor to connect broken or unresolved property tongues owing to the small spatial scales of dense water overflows, mid-ocean fracture zones, and episodic property transport. In particular, bottom flow is parameterized for those boxes poorly described by their immediate neighbors by searching over successively larger bottom areas for potential sources, beginning with a 2° radius and then incrementally increasing up to 16°, which we will show is sufficient to describe all bottom points in the datasets employed here.

Second, the ocean is not in a strict steady state. To minimize the influence of seasonality, we apply TMI to observations that represent late wintertime conditions by requiring that the ocean be well-mixed above the seasonally-maximum mixed-layer depth, reflecting the fact that this depth is most indicative of the properties transmitted into the ocean interior [*Stommel*, 1979]. Here we use the properties found at the base of seasonal mixed layer in order to define the *surface* properties that get transmitted into the ocean interior [*Stommel*, 1979]. A further issue is that disequilibrium between the surface and deep ocean is expected due to both natural ocean-atmosphere variability and anthropogenic changes [*Johnson and Orsi*, 1997; *Huang et al.*, 2003; *Curry and Mauritzen*, 2005; *Levitus et al.*, 2005; *Jacobs*, 2006; *Gouretski and Koltermann*, 2007]. Water-mass properties have changed in time [*Yashayaev and Clarke*, 2008], suggesting that TMI may not follow property tongues to their exact surface origin, but

the properties of different ocean basins are far more distinct than any observed changes in the instrumental record, suggesting that the solution will not be strongly biased. We proceed with the steady-state assumption as a provisional first-order description of the ocean, subject to posterior checks of the extent that non-steady behavior has distorted the solution.

The surface boundary conditions must be interpreted correctly. Note that contact with the atmosphere does not necessarily imply complete equilibration of a water type with overlying atmospheric conditions so that water properties may be indicative of exchanges at multiple locations, though for purposes of specificity we focus on the most recent exchange.

2. Estimating tracer distributions

It is necessary to determine if the global cost function has been sufficiently minimized. To determine whether the steady-state pathways are consistent with the tracer climatologies, we formulate a subset of the global cost function for each tracer type:

$$\mathrm{J}_c = (\mathbf{Ec} - \mathbf{c}_{obs})^T (\mathbf{Ec} - \mathbf{c}_{obs}), \tag{3}$$

where $\mathbf{c}$ is a vectorized tracer distribution with observations $\mathbf{c}_{obs}$, and all tracers have been rendered independent by the linearization step above. The computation of J_c, however, involves uncertain surface boundary conditions. If changes to the surface boundary conditions are expressed as a control vector $\mathbf{u}$, the steady-state circulation can be represented as:

$$\mathbf{Ac} = \mathbf{d} + \Gamma\mathbf{u}, \tag{4}$$

where $\mathbf{d}$ is a vector that contains the surface boundary conditions and interior sources and sinks and Γ is a matrix that maps the control vector into the proper parts of $\mathbf{d}$.

Inverting equation (4) and substituting into (3), we have:

$$\mathrm{J}_c = (\mathbf{E}\mathbf{A}^{-1}\mathbf{d} + \mathbf{E}\mathbf{A}^{-1}\Gamma\mathbf{u} - \mathbf{c}_{obs})^T(\mathbf{E}\mathbf{A}^{-1}\mathbf{d} + \mathbf{E}\mathbf{A}^{-1}\Gamma\mathbf{u} - \mathbf{c}_{obs}). \quad (5)$$

We can redefine the terms and write J solely as a function of **u**:

$$\mathrm{J}_c = \mathbf{u}^T\mathbf{H}\mathbf{u} + 2\mathbf{f}^T\mathbf{u} + \mathbf{r}^T\mathbf{r}, \quad (6)$$

where

$$\mathbf{H} = \Gamma^T\mathbf{A}^{-T}\mathbf{E}^T\mathbf{E}\mathbf{A}^{-1}\Gamma, \;\; \mathbf{f}^T = \Gamma^T\mathbf{A}^{-T}\mathbf{E}^T\mathbf{r}, \;\; \mathbf{r} = \mathbf{E}\mathbf{A}^{-1}\mathbf{d} - \mathbf{c}_{obs}. \quad (7)$$

Taking the partial derivative of J_c with respect to **u** and setting to zero, we can solve for the **u**, and hence **c**, that best fits the data:

$$\mathbf{u} = -\mathbf{H}^{-1}\mathbf{f}. \quad (8)$$

A first test is to see whether the estimated temperature, salinity, δ^{18}O, phosphate, nitrate, and oxygen fields are within their expected observational tolerances. In this case, the **E** matrix above is replaced with the identity matrix because we have complete gridded datasets. We find that all of the tracers are estimated within the published error estimates. After normalizing to make the expected J value for each tracer to be 1, we find that J equals 0.34 for temperature, 1.46 for salinity, 0.02 for δ^{18}O, 0.32 for phosphate, 0.67 for nitrate, and 1.22 for oxygen (see Fig. S1). The δ^{18}O dataset provides a rather weak constraint because of the large published errors relative to the water-mass signal [*Legrande and Schmidt*, 2006]. The actual error in δ^{18}O is probably smaller than we have used, so the overfitting of the data is not as bad as the J value makes it appear.

The TMI method allows the estimation of tracer distributions which were not used to obtain the **A** matrix, such as δ^{13}C. The use of withheld data to check the estimated steady-state

pathways represents a more stringent test, obviously. In this case, $\mathbf{E}$ transfers the δ^{13}C vector $\mathbf{c}$ from the WOCE hydrographic climatology grid onto the locations of the withheld data, $\mathbf{c}_{obs}$. Figure 1 of the main manuscript shows the results of this test, where the standard deviation of the misfit between estimated and observed carbon-13/carbon-12 isotope ratio is 0.2 per mil, an acceptable value.

3. Diagnosing water-mass pathways

If $\mathbf{c}$ is set to one in a surface patch of interest and zero elsewhere, the global distribution of the tracer $\mathbf{c}$ is found by inverting $\mathbf{A}$, i.e., $\mathbf{c} = \mathbf{A}^{-1}\mathbf{d}$. In practice, $\mathbf{A}^{-1}$ is not explicitly computed, but an LU factorization is used to calculate the product of $\mathbf{A}^{-1}$ and any vector. The resulting tracer distribution indicates the fraction of mass that has originated from that surface location [*Khatiwala et al.*, 2001; *Haine and Hall*, 2002].

The ability to accurately distinguish waters originating from nearby regions can be assessed by comparing the 2^o and 4^o resolution solutions. We find that the total amount of volume originating from the regional patches defined by Gebbie and Huybers (2010) is similar to within 2% between the two solutions, with the only exception being the ratio of Ross to Weddell Sea Waters. While the total amount of Antarctic Water is the same in both solutions, 36% of the global total, the breakdown of Weddell to Ross Sea Waters is different. In the 2° solution, Ross Sea Water is the origin of 20% of the global volume, but the 4° solution indicates that the Ross Sea is the origin of just 14% of global volume. In general, we find that zonal averages are insensitive to the resolution of the datasets.

4. Adjoint method for the surface origination map

Following the diagnosis of a water-mass pathway, the total volume of the interior ocean originating from a given surface box is then calculable as the sum of the volume of each box multiplied by the mass fraction dye tracer **c**:

$$V = \mathbf{v}^T \mathbf{c}, \tag{9}$$

where **v** is a vector of the volumes of each grid box. To make a global map of the amount of ocean volume originating from each location, one needs to calculate a complete **c** distribution for each of the 11,113 surface locations.

Substituting the value of **c** from the forward model equation, i.e., $\mathbf{c} = \mathbf{A}^{-1}\mathbf{d}$ into (9), we get:

$$V = \mathbf{v}^T \mathbf{A}^{-1} \mathbf{d}. \tag{10}$$

Now the sensitivity of V to changes in the boundary conditions can be solved with one inversion of the transpose of **A**:

$$\frac{\partial V}{\partial \mathbf{d}} = \mathbf{A}^{-T} \mathbf{v}, \tag{11}$$

where $-T$ refers to the inverse transpose of the matrix and the partial derivative is equal to $\mathbf{V}_{tot}$ in the main text. The terms of the resulting sensitivity vector that correspond to the surface give the change in volume for a given change in the surface boundary condition. This is exactly a map of the volume of the global ocean that has originated from each of the surface locations. This equation can also be found by the method of Lagrange multipliers (or an *adjoint method*), whereby we also arrive at the inverse of the transpose **A** matrix being important. This equation can be solved in just one matrix-vector product, a more efficient means of obtaining sensitivity

information. This calculation is used to produce the results shown in Figure 2 of the main text.

5. The distribution of water masses and its sensitivity to spatial resolution and noise

The distribution of water masses is easily diagnosed by taking the elements of $\partial V/\partial \mathbf{d}$ above that correspond to surface locations, then sorting them by relative size. The distribution is computed by using both the WOCE hydrographic climatologies at 2° and 4° horizontal resolution. When the 2° distribution is downscaled to 4°, the results are very similar (Fig. S3), and it appears that the solution characteristics are not a strong function of resolution.

Figure 3 of the main manuscript finds a near '-1' power law in the distribution of surface contributions. A simple tracer advection-diffusion model of an overturning circulation suggests a possible explanation. The simple setup is two-dimensional in the -yz plane with 25×25 gridpoints. A simple streamfunction has all of the downwelling occurring along the boundary with upwelling occurring everywhere else. We find that the slope of power law is proportional to the Peclet number. In essence, the power law provides an estimate of the entrainment that occurs during the downwelling limb of the overturning circulation.

Two other robustness tests are worthy of note. In an experiment in which uncorrelated noise with the magnitude of observational error is added to the actual observations, the first step (local step) of the TMI method cannot find a viable steady-state circulation to explain the data in over 50% of the points. This is contrast to the observations without additional noise, where the local step can satisfy the observations without error in over 99% of locations. Even though most of the local inversions are further out of balance than acceptable (in the

noise-added case), we can nonetheless proceed to the second step of a global inversion. Here we find, after completing the second step, that the reconstructed tracer fields are little perturbed by the additional noise. Apparently, the global inversion is able to filter out much of the local noise. These results hold the further opportunity that we can likely identify how far out of balance the present ocean circulation is. We also note that the ocean climatologies have been extensively averaged, and this likely makes it easier for TMI to find a steady-state solution.

In a second test, we used synthetic tracer data produced by S. Khatiwala from a steady-state version of the MIT General Circulation Model [*Khatiwala et al.*, 2005], with a known water-mass distribution that was treated as the "truth". Applying the TMI method to the synthetic observations, we recovered the GCM-modeled water-mass decomposition with an error of less than 5% in the deep ocean, and not larger than 10% in the upper ocean. The results of these tests suggests that the TMI method is robust.

Acknowledgment. We thank an anonymous reviewer for simplifying the derivation of the adjoint calculation for surface origins.

References

Curry, R., and C. Mauritzen (2005), Dilution of the northern North Atlantic Ocean in recent decades, *Science*, *308*(5729), 1772–1774.

Gebbie, G., and P. Huybers (2010), Total matrix intercomparison: a method for resolving the geometry of water-mass pathways, *J. Phys. Oceanogr.*, *40*(8), 1710–1728.

Gouretski, V., and K. Koltermann (2004), WOCE Global Hydrographic Climatology, *Tech. Rep. 35*, Berichte des Bundesamtes für Seeschifffahrt und Hydrographie.

Gouretski, V., and K. P. Koltermann (2007), How much is the ocean really warming?, *Geophysical Research Letters*, *34*(1).

Haine, T. W. N., and T. M. Hall (2002), A generalized transport theory: Water-mass composition and age, *J. Phys. Oceanogr.*, *32*(6), 1932–1946.

Hansen, P. C. (1992), Analysis of discrete ill-posed problems by means of the L-curve, *Siam Review*, *34*(4), 561–580.

Huang, B., P. Stone, A. Sokolov, and I. Kamenkovich (2003), The Deep-Ocean Heat Uptake in Transient Climate Change, *Journal of Climate*, *16*(9), 1352–1363.

Jacobs, S. (2006), Observations of change in the Southern Ocean, *Philosophical Transactions of the Royal Society A: Mathematical, Physical and Engineering Sciences*, *364*(1844), 1657–1681.

Johnson, G. C., and A. H. Orsi (1997), Southwest Pacific Ocean water-mass changes between 1968/69 and 1990/91, *Journal of Climate*, *10*(2), 306–316.

Khatiwala, S., M. Visbeck, and P. Schlosser (2001), Age tracers in an ocean GCM, *Deep-Sea Research I*, *48*(6), 1423–1441.

Khatiwala, S., M. Visbeck, and M. A. Cane (2005), Accelerated simulation of passive tracers in ocean circulation models, *Ocean Modelling*, *9*(1), 51–69.

Legrande, A. N., and G. A. Schmidt (2006), Global gridded data set of the oxygen isotopic composition in seawater, *Geophysical Research Letters*, *33*(12).

Levitus, S., J. Antonov, and T. Boyer (2005), Warming of the world ocean, 1955-2003, *Geophysical Research Letters*, *32*(2).

Schlitzer, R. (2007), Assimilation of radiocarbon and chlorofluorocarbon data to constrain deep and bottom water transports in the world ocean, *Journal of Physical Oceanography*, *37*(2), 259–276.

Stommel, H. (1979), Determination of water mass properties of water pumped down from the Ekman layer to the geostrophic flow below, *Proc. Natl. Acad. Sci.*, *76*, 3051–3055.

Yashayaev, I., and A. Clarke (2008), Evolution of North Atlantic water masses inferred from Labrador Sea salinity series, *Oceanography*, *21*(1), 30–45.

Received _____

Figure 1.

Figure 2.

Figure 3.

Figure Captions

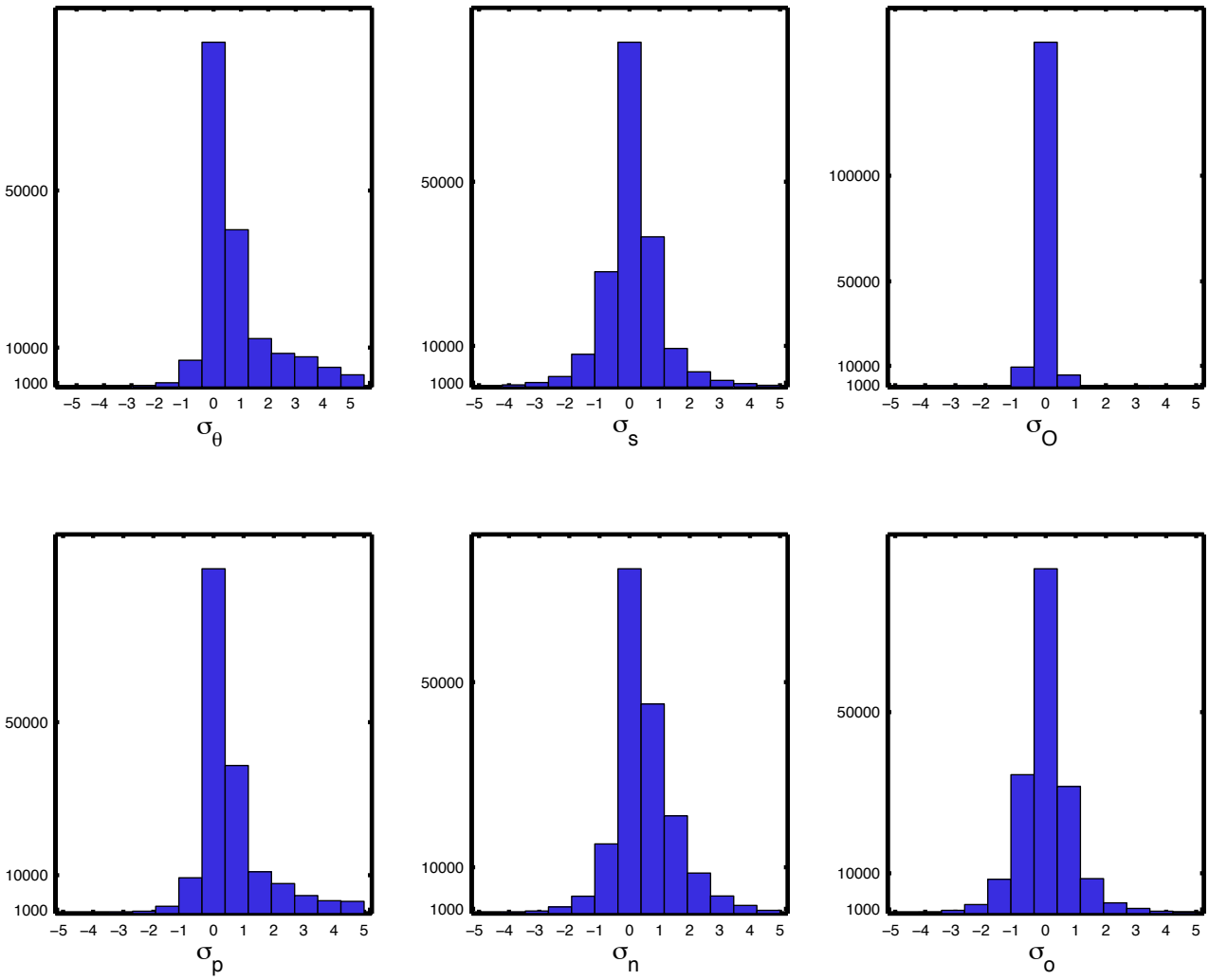

Figure 1. Histograms of the misfit between the TMI surface-boundary solution and observations for potential temperature (*top left*), salinity (*top middle*), $\delta^{18}O$ (*top right*), phosphate (*bottom left*), nitrate (*bottom middle*), and oxygen (*bottom right*). In all cases, the misfits have been divided by the published error in the climatological tracer fields and are reported in standard deviations.

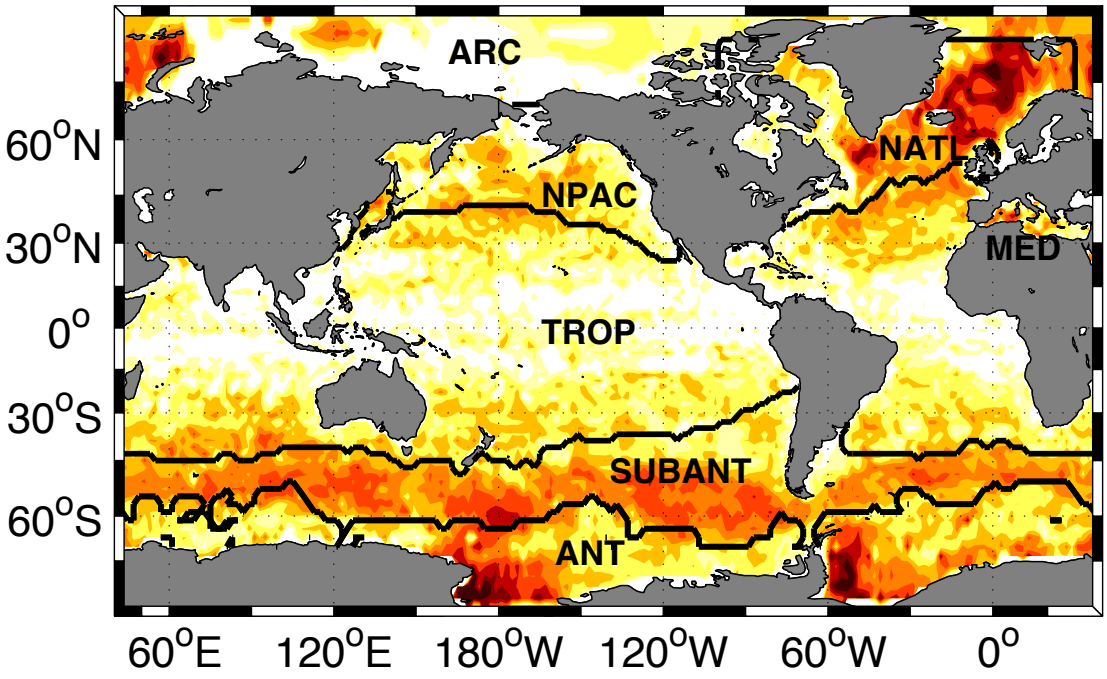

Figure 2. Ocean surface divided into seven surface regions (ANT = Antarctic Water, NATL = North Atlantic Water, SUBANT = Subantarctic Water, NPAC = North Pacific Water, ARC = Arctic Water, MED = Mediterranean Water, TROP = Tropical and subtropical waters).

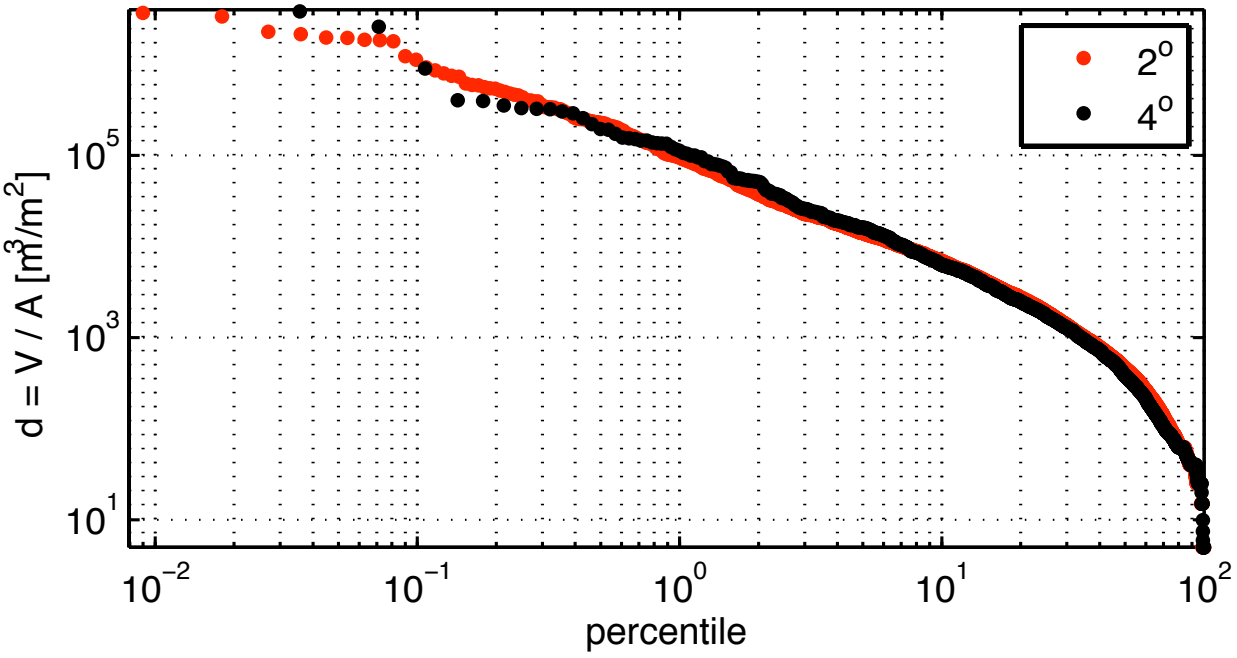

Figure 3. Comparing the distribution of water masses as calculated at 4° horizontal resolution (*black dots*) and as calculated at 2° resolution (*red dots*). The volume of the global ocean originating from each surface site is plotted in order of importance. The ranking of points is put into percentile to facilitate the comparison of the two resolutions.